Spectroscopic Fingerprints of MgCl2/TiCl4Nanoclusters Determined by Machine Learning and DFT

Spectroscopic Fingerprints of $MgCl_2/TiCl_4$ Nanoclusters Determined by Machine Learning and DFT

Maddalena D'Amore*,[1] Gentoku Takasao,[2] Hiroki Chikuma,[2] Toru Wada,[2] Toshiaki Taniike*,[2] Fabien Pascale,[3] and Anna Maria Ferrari[1]

[1]*Dipartimento di Chimica, Università di Torino, Via P. Giuria 5, 10125 Torino, Italy*

[2]*Graduate School of Advanced Science and Technology, Japan Advanced Institute of Science and Technology, 1-1 Asahidai, Nomi, Ishikawa, 923-1292, Japan*

[3]*Université de Lorraine - Nancy, CNRS, Laboratoire de Physique et Chimie Théoriques, UMR 7019, Vandoeuvre-les-Nancy, France*

(Dated: August 24, 2021)

Abstract

Understanding the structure and properties of $MgCl_2/TiCl_4$ nanoclusters is a key to uncover the origin of Ziegler-Natta catalysis. In particular, vibrational spectroscopy can sensitively probe the morphology and active species of $MgCl_2/TiCl_4$. Here, we determined vibrational spectroscopic fingerprints of $50MgCl_2$ and $50MgCl_2/3TiCl_4$ which were obtained by non-empirical structure determination based on an evolutionary algorithm and DFT. The adsorption of CO, $TiCl_4$ and Ti_2Cl_8 dimers was also modelled on each of coordinatively unsaturated Mg^{2+} sites available for binding including so-called defect sites, which are likely present at the surface of activated $MgCl_2$ nano-crystals and plausible sites for strong $TiCl_4$ species adsorption. The outcomes of thermodynamical and vibrational analysis were compared to results on ideal surfaces of $MgCl_2$. Vibrational analysis (IR and Raman) on plausible models of $TiCl_4$/ $MgCl_2$ nanoclusters revealed that IR response is useful to distinguish between the different ways of binding of $TiCl_4$ on different sites of adsorption, whereas Raman response provides a clear fingerprint of supported $TiCl_4$ species.

Keywords: polymerization catalysis, machine learning, nanoclusters, DFT, Raman spectrum, IR spectrum

I. INTRODUCTION

The structural unit of the Ziegler-Natta catalyst (ZNC) is nanostructured and disordered $MgCl_2$ whose lateral surfaces are capped by $TiCl_4$ and Lewis bases (called internal donors). Such an active structure is obtained by forming or reconstructing $MgCl_2$ in the presence of $TiCl_4$ and/or internal donors during catalyst preparation. The ball-milling of highly crystalline $MgCl_2$ or transformation of a $MgCl_2$ precursor such as $Mg(OEt)_2$ yields disordered δ form of $MgCl_2$. Given experimental difficulties in characterizing this catalyst, computational approaches have provided a great contribution to the overall understanding of δ-$MgCl_2$ (and of $MgCl_2$-based ZN catalysts in general), because of the feasibility of modelling the isolated contribution of single surfaces or catalytic sites.[1] Theoretical chemistry due to advances in quantum chemistry, in particular in the Density Functional Theory (DFT) has been decisive in last decades for this field of research. Shortly, the seminal $MgCl_2$ models as obtained from molecular mechanics in the 1980s presented the (110) and (104) lateral surfaces as the putative surfaces for the adsorption of monomeric and stereo-selective dimeric Ti_xCl_y species, respectively.[2] However, more recent DFT studies have claimed the crisis of those models, warning about the critical thermodynamic stability of Ti_x Cl_y species on flat and regular $MgCl_2$ surfaces, and moving towards a much more complex morphology of the δ-$MgCl_2$ particles.[3–11] Recent theoretical calculations on $MgCl_2$ bulk and surface structure by means of periodic Density Functional Theory methods including dispersion (DFT-D*) predicted that well-formed $MgCl_2$ crystals in the absence of adsorbates predominantly feature the (104) surfaces, however, the situation drastically changes in the presence of adsorbates (including electron donors). DFT-D simulations[12,13] demonstrated that $MgCl_2$ crystals mainly expose the (110) surfaces when they are formed in the presence of Lewis bases (especially small molecules such as methanol, ethanol, and dimethyl ether) or in presence of alkoxy silanes adopted as external donors. The application of Bravais' law allowed the identification by some of us of thermodynamically most stable surfaces and the construction of a comprehensive set of slabs as model surfaces of increasing stability in terms of surface Gibbs Free Energy namely (107), (012), (101), (015) and (110) ones.[14] Nano-size and crystallite shapes are key features of many catalysts and, among others, the morphology of the primary particles and details of exposed surfaces of $MgCl_2$-based Ziegler-Natta catalysts for olefin polymerization still remain experimentally inaccessible. Together with detailed structural

analysis of the supporting δ-$MgCl_2$ nanoparticles by synchrotron X-ray total scattering[15] , the construction of the Wulff's plot of the whole $MgCl_2$ particles revealed that ball-milling of naked $MgCl_2$ not only promotes an increase in the total surface area, but also changes the relative extension of the surfaces, favoring the formation of the lateral surfaces exposing strongly acidic Mg^{2+} sites (i.e., the (110), (012) and (015) ones) at the expenses of the basal (001) one. Moreover, theoretical calculation predicted the existence of several possible edges involving the (110) surface.[16] Such inter-surfaces edges are remarkably relevant because in some recent theoretical models they were advocated as the favorable place for stereo-selective active sites.[17] The morphology and surface properties of δ-$MgCl_2$ nanoparticles (i.e. the relative extension of the exposed surfaces) have been elucidated by vibrational spectroscopies for a series of mechanically and chemically activated $MgCl_2$ samples, and by building up a comprehensive set of model structures (both ordered and disordered) in order to highlight nanosizing effects. Far-IR spectroscopy coupled with quantum-mechanical simulations and complemented by mid-IR spectroscopy of CO adsorbed at 100 K gave a comprehensive picture of the morphology of $MgCl_2$ nano-particles and of their surface properties. More recently, different nanostructures were obtained in terms of disorder and morphology, which in turn influence the overall catalytic performance. The investigation was further extended by looking at the lattice dynamics of $MgCl_2$ systems by means of Inelastic Neutron Scattering (INS) spectroscopy,[18] which is a valuable method to probe the motion of atoms within a material and hence understand the structural disorder of nano-sized systems. In recent years, some of the authors have sharpened the use of FT-IR spectroscopy of adsorbed carbon monoxide as a technique to get information on the $MgCl_2$ exposed surfaces and their relative extent.[14,19] The method, which was attempted for the very first time by Zakharov and co-workers[20], was demonstrated to be particularly powerful, especially when the $MgCl_2$ surfaces are not fully occupied by the other components and/or by side residues of the synthesis. This technique efficiently reveals the type and amount of exposed Mg^{2+} sites, which in turn are correlated with the extension of specific lateral surface.[14]

In this work, model nanoplates ($50MgCl_2$ and $50MgCl_2/3TiCl_4$) were obtained by non-empirical structure determination based on the genetic algorithm and DFT, which was developed by some of us.[21,22] The exposed surfaces and the defective sites contained in these 'realistic' models were probed by CO adsorption to identify weakly acidic Mg^{2+} cations and strongly acidic Mg^{2+} cations. The obtained vibrational behavior was compared with that

emerged in the 2D periodic treatment for surfaces and 'classical' clusters built by Wullffs' polar plots. So far, various computational methodologies have been adopted to explore stable docking sites for $TiCl_4$ and its dimeric species but the calculations were mostly based on the assumption of ideal or simplified clusters of $MgCl_2$. Going beyond the too simplified surface models present in literature, here we adopted well assessed DFT methodology previously employed for surfaces, while stepped forward to a more realistic model of $MgCl_2$ nanoclusters by means of the non-empirical structure determination. On these nanostructures we carried out vibrational Far-IR and Raman analysis to discuss to which extent exposed tetra and penta Mg sites are distinguishable and, even more interestingly, the possibility to recognize: i) the effect of adsorption of different precatalytic complex Ti_xCl_y on IR and/or Raman bands, ii) to what extent it is possible to distinguish between Ti_xCl_y species on the basis of features occurring in IR and/or Raman spectra; that with the aim to discuss whether or not it is possible to obtain a vibrational evidence of the presence of a precatalytic species on a specific site. With this target in mind, we identified spectroscopic IR features and more evidently Raman bands specific of each adduct as possible fingerprints of Ziegler-Natta catalysts.

II. COMPUTATIONAL MODELS AND DETAILS

A. Machine Learning construction of nanoplate

Non-empirical structure determination was performed for $50MgCl_2$ and $50MgCl_2/3TiCl_4$ on the basis of a program that combines global structure search using a genetic algorithm and local geometry optimization using DFT.[21,22] The size of $50MgCl_2$ is about 3 nm in diameter, consistent with the experimentally observed size of the primary particles (ca. 2.4-4.0 nm).[15] Three $TiCl_4$ molecules with respect to 50 $MgCl_2$ units correspond to 2.69 wt%, similar to a typical Ti content of industrial Ziegler-Natta catalysts.[23] The structure determination program assumes a convex $MgCl_2$ monolayer with its lateral surfaces capped by $TiCl_4$. A $MgCl_2$ skeleton consists of N Mg^{2+} cations and 2N Cl^- anions respectively placed at atomic positions in the ionic crystal, where the Cl^- anions are placed in the descending order of the coordination number. Adsorption sites were defined on the lateral periphery of the $MgCl_2$ skeleton. The $TiCl_4$ adsorption occurs in a way that a Ti^{4+} cation

becomes hexacoordinated or pentacoordinated, e.g., mononuclear species on {110} surfaces, and mononuclear and dinuclear species on {104} surfaces. The structures are subjected to DFT geometry optimization, and evolved through genetic operators, where the energy of the optimized structures is used to derive the fitness. As in our previous works,[21,22,24] the DFT geometry optimization was performed using DMol3 at a level of GGA PBE as the exchange-correlation functional, and the double-numerical basis set with polarization functions (DNP) and effective core potential (ECP). Further details are given in literature.[21,22]

B. DFT calculations

The DFT[25,26] calculations reported in this paper were mainly based on the B3LYP global hybrid functional,[27,28] as implemented in the CRYSTAL program.[29,30] Since dispersion plays a key role in the investigated chemical systems the semi-empirical DFT-D2 approach based on Grimme's empirical correction[31,32] was adopted in combination with the hybrid B3LYP functional; that combined scheme have been found to successfully describe surface interactions.[33,34] PBE0-D3 (including three bodies correction) adsorption energies, together with the outcomes of a non local meta-GGA by Truhlar have been also reported as Supplementary Information for plausible precatalytic Ti_xCl_y species on the nanocrystal.

Split valence triple-zeta basis sets plus polarization (TZVP) of Gaussian type functions have been adopted for all the elements (Mg, Ti and Cl atoms).[9] For most of the surfaces the adsorption of CO has been modeled adopting the same level of calculation described above and also an Ahlrichs QTZV plus polarization (QTZVP2) quality basis set. The coefficients of the polarization Gaussian functions (α_{pol}) were optimized in a previous study on adsorbed CO.[35]

To inspect the molecular vibrational shifts of CO and $TiCl_4$ due to the interaction with the support, we performed geometry optimizations followed by harmonic vibrational frequency calculations (and the corresponding IR and Raman intensities) of the molecular adducts. Thermodynamic properties have been computed at standard conditions (P = 1 bar, T = 298 K) and additionally at T= 100 K. Details concerning the computational set up and the calculations of the vibrational frequencies are collected in the Supplementary Information Section.

III. RESULTS AND DISCUSSION

A. Structure, morphology of nanoplates

The structures of $50MgCl_2$ and $50MgCl_2/3TiCl_4$ were determined using a non-empirical structure determination program developed and modified by some of us.[21,22] $50MgCl_2$ was adopted, considering that the surface extensions and far-IR are size sensitive. Its size (ca. 3 nm) is comparable to the known size of the primary particles (2.4-4.0 nm). Note that $50MgCl_2$ is much larger than $19MgCl_2$, the largest structure determined in the previous papers,[21,22] and therefore is computationally quite demanding because of the intrinsic cubic scaling of DFT and an exponential increase of the possible configuration space. Figure 1 shows evolutionary progress plots for the structure determination of $50MgCl_2$ and $50MgCl_2/3TICl_4$, respectively. The energy of the best-of-generation structure decreased as a result of evolution. The high computational cost impeded multiple runs implemented over a sufficient number of generations, i.e., the global minima were not guaranteed. Nonetheless, (however, as expected from our experiences in smaller clusters), the obtained structures exhibited features similar to those of the most stable structures for smaller $MgCl_2/TiCl_4$ systems.[21] As shown in Figure 2b, bare $MgCl_2$ dominantly exposed {104} or analogous surfaces as lateral surfaces exposing the most stable pentacoordinated Mg^{2+} to minimize the coordinative vacancy. Besides, two terminal Cl^- anions were symmetrically placed at Mg^{2+} corners situated in a tetrahedral symmetry. In the presence of $TiCl_4$, the structure of $MgCl_2$ was reconstructed in a way to expose {110} surfaces, and the {110} surfaces were necessarily capped by the $TiCl_4$ molecules (Figure 2a).

Only monomeric species, $TiCl_4$ bound the stronger undercoordinated Mg^{2+} was formed since the low concentration of $TiCl_4$ (the Mg to Ti molar ratio is 50:3) prevents the formation of $TiCl_4$ aggregates. This finding is in line with previous indications from Zerbi et al. (see Ref.[36]) and with the energy estimates reported in Refs. 9 and in Table S1 of Supported Information. Nevertheless, the fractions of the Ti_2Cl_8 dimer and penta-coordinated $TiCl_4$ at P sites are not completely negligible, but much smaller than that of the hexacoordinated $TiCl_4$ at T sites. The fractions decrease of course along with the decrease in the Ti content. Bare $50MgCl_2$ (hereafter simply referred to as $MgCl_2$) and $50MgCl_2/3TiCl_4$ nanoplates as derived from machine learning algorithm are sketched in Figure 1. For sake of clarity and because

of its relevance in the following discussion, the cluster obtained from $50MgCl_2/3TiCl_4$ after removal of the three $TiCl_4$ (hereafter referred to as $MgCl_2$*) is also reported in the Figure. The size of a nanocluster is about $37\mathring{A} \times 25\mathring{A}$.

The distribution of Mg^{2+} ions in their different coordinations is described in Table 1 where pentacoordinated Mg^{2+} ions typical of (012), (104), (015) surfaces are denoted as P sites and tetracoordinated Mg sites typical of (110) surfaces as T sites. In the bare nanoplate the tetracoordinated Mg^{2+} ions (T) are about the 8 % of total exposed sites and are all isolated sites; in $50MgCl_2^*$ the tetracoordinated Mg^{2+} ions amount to about 14 % (i.e.36.8% of total exposed sites) and mainly composed by couples of vicinal T sites; the hexacoordinated Mg^{2+} ions form the largest part of total Mg^{2+} ions amounting to 62%; the last part is formed by pentacoordinated Mg^{2+} ions that forms 20% of the total sites; the minority of 4% of tetrahedral sites closes the list, see Table 1. The increase in the fraction of the T sites in $MgCl_2^*$ occurs mainly at the expense of the P sites and to the extent that this occurs, it is therefore the coordination of $TiCl_4$ that dictates the final shape of the nanoparticles.

The P sites belonging to different surfaces (listed above) can be easily identified in infinite models, but due to the finite nature of the clusters we cannot distinguish (or not properly can distinguish) different P sites present on nanoplatelet terminations.

The occurrence of tetracoordinated Mg sites mainly upon reconstruction in presence of $TiCl_4$ supports the finding that in microcrystal the presence of the related (110) surface accounts for 1.4 % of the total exposed surface by means of previous Wulff polyhedron simulations.[16] The existence of several edges due to the combination of adjacent faces[37,38], such as the (110)/(104), (110)/(012) and (110)/(015) were identified as possible interest for catalysis. In particular, the former (110)/(104) edge have been recently considered as a privileged site for strong $TiCl_4$ adsorption to generate a stereo-selective active site[10,17] bringing tetracoordinated sites (T) close to pentacoordinated (P) ones; also in our models of $MgCl_2$ support the T sites with attached $TiCl_4$ molecules lie close to P sites.

Relative stabilities of nanoplates is evaluated by considering the cluster formation reaction starting from bulk $MgCl_2$ and gas phase $TiCl_4$; the relative energy, $E_{cluster}$, has been computed from the calculated energy of a structure (E) according to the formula

$$E_{cluster} = E - N_{MgCl_2} \cdot E_{MgCl_2} - M_{TiCl_4} \cdot E_{TiCl_4} \quad (1)$$

where N_{MgCl_2} indicates the number of formula unit of α-$MgCl_2$ bulk and E_{MgCl_2} the relative electron energy whereas, M_{TiCl_4} is the number of $TiCl_4$ molecules adsorbed on cluster with relative energy E_{TiCl_4} in gas phase.

Following the GA evolution (see Figures 1), $50MgCl_2/3TiCl_4$ is more stable than the $50MgCl_2$ bare nanocluster by about 170 kJ/mol. Thus the energy penalty to reconstruct in order to expose T sites (33 kJ/mol) is largely compensated by the $TiCl_4$ adsorption energy (-203 kJ/mol, corresponding to -67.7 kJ/mol for each $TiCl_4$), PBE results. PBE0-D3 calculations on the same clusters (including three bodies correction) provide a similar picture with a stabilization predicted in about 238 kJ/mol that is perfectly reasonable due to the inclusion of dispersion correction.

B. Surface Lewis acidity of $MgCl_2$ nanoplatelet: probing by CO

Nanoplates presented in this work simulates nanostructured $MgCl_2$. Even still at the lower side of dimensional range of typical industrial samples it is large enough to show all possible catalytic sites. To characterize the Lewis acidity of the different exposed lateral sites in the nanoplate (exposed Mg^{2+} sites either belong to small terraces or are close to edges connecting different surfaces), the adsorption of CO on $MgCl_2$* (with many different sites available for adsorption) has been studied. The proposed models of CO bound to different edge sites of the nanoplatelet are reported in Figure 3. The site indicated as A corresponds to a tetracoordinated Mg^{2+} ion of the kind exposed by (110) surfaces but close to a tetrahedral Mg^{2+} one. In the panel B of the same figure, the tetracoordinated Mg^{2+} ion is the one typical of (110) families of surfaces i.e. close to another analogous tetracoordinated Mg^{2+} ion but on the other side close to a row of pentacoordinated Mg^{2+} ions that is at the edge of the type (110)/(104). Panel C hosts the model for a CO molecule adsorbed on a tetrahedral Mg^{2+} ion; the D model represents a CO molecule adsorbed on a pentacoordinated Mg^{2+} ion but still at the edge pentacoordinated Mg^{2+}/tetracoordinated Mg^{2+} whereas the model E reports the adsorption on a pentacoordinated Mg^{2+} of the kind of sites of both (104) and (107) families of planes. Finally, to see whether CO frequency can be perturbed by a $TiCl_4$ adsorbed in the proximity, CO has been adsorbed at an edge of the type (110)/(104), sharing the T site with $TiCl_4$ (model F).

All data are collected in Table 2 including (only for binary CO/$MgCl_2$ systems) results from regular surfaces exposing Mg atoms with the same coordination number (from periodic 2D calculations). In this latter case isolated CO adsorption (degree of coverage equal to 0.25) has been considered for a one-to-one comparison with the nanoplate sites.

The thermochemical analysis performed at 100 K reveals that, in agreement with the experimental observation, the CO adsorption energy is rather weak on all the sites also at 100 K and, as expected, the interaction is stronger with the tetra-coordinated ones. The Gibbs free energy of adsorption, ΔG_{ads} is about -25 kJ/mol on sites A, B and about -20 kJ/mol on sites D and E. The difference between tetra and pentacoordinated site is indeed small (less than 5 kJ/mol) but enough to recognize a significantly different chemical response from the two types of Mg^{2+} ions.

The formation of mono-carbonyl species is characterized by a relevant polarization that red shifts the CO stretching frequency. $\Delta\nu$ is 74 cm^{-1} for sites A and B and $\sim$ 62 cm^{-1} for sites D and E respectively (they differ only by 2 cm^{-1}). Thus, these two groups of sites exhibit different Lewis acidity, and as expected T Mg^{2+} are stronger Lewis acid than the P ones. The CO red shift is 72 cm^{-1} for site F, in this case we can argue that due to polarizing effect of adsorbed $TiCl_4$ the pentacoordinated Mg^{2+} behaves as the sites A and B instead of P type sites as proved by both the enthalpy (ΔE_{ads} = -42.3 kJ/mol) and the shift in CO ($\Delta\nu$=71.3 cm^{-1}) absorption frequency. That may justify the fact that, after reaction with $TiCl_4$, the IR absorption band falling at high wavenumbers and assigned to CO adsorbed on highly polarizing surfaces (i.e. (110), (015), and/or on the (012) surface) greatly decreases in intensity but it does not disappear completely, maybe due to the presence of local adducts indicated as type F in Fig.3.

On regular surfaces the trend on energies and frequencies is similar to that found for the nanocluster: ΔG_{ads} is about -18/-14 kJ/mol on 107 and 104 surfaces (D and F sites) and $\sim$ -14.5 kJ/mol on 110 planes (A and B sites). $\Delta\nu$ is $\sim$ 54 cm^{-1} on 107 and 104 surfaces and $\sim$ 64 cm^{-1} on 110. $\Delta\nu$ for CO adsorbed at T nanoplate sites is larger than that obtained on a surface homologous (110) by about 15 cm^{-1} (both the A and B sites behaves that way), while by about 8-10 cm^{-1} for P nanoplate sites as compared to the shift on (107) and (104).

On the basis of presented results we can conclude that CO molecules on nanoplates:

i) can successfully probe T sites but cannot distinguish between T sites in different environments (i.e. between isolated or adjacent sites); in addition in the presence of $TiCl_4$, the

stretching frequency of a CO molecule adsorbed in its proximity is close to a signal from a T site (they differ by 2 cm^{-1}); that justifies the fact that after reaction with $TiCl_4$, the IR absorption band falling at high wavenumbers and assigned to CO adsorbed on highly polarizing surfaces (i.e. (110), (015), and/or on the (012) surface) greatly decreases in intensity but it does not disappear completely, maybe for the presence of local adducts indicated as type F in Figure 3;

ii) the non-negligible increases of adsorption energies and frequencies values on nanoplate sites, reveal the presence of stronger acidic sites on highly nanostructured support of activated catalysts with respect to the homologous surface sites.

For sake of completeness, the adsorption on site C (tetrahedral Mg^{2+}) has been also modeled although tetrahedral terminations did not emerge in surface studies.

C. IR and Raman response of $TiCl_4$ on nanoplatelet: naked vs. covered

We considered the naked nanoplatelet and the $50MgCl_2/3TiCl_4$ adduct obtained by GA, the platelet $MgCl_2$* and its $TiCl_4$ on site B and both Ti_2Cl_8 and $TiCl_4$ on site E. All that aiming at a reexamination of the mononuclear adsorption of $TiCl_4$ on (110) $MgCl_2$ surfaces, the mononuclear on $MgCl_2$ (104), as well as dinuclear adsorption on $MgCl_2$ (104); the last three cases correspond to those proposed by Corradini as possible precursors of active species. For all the above-mentioned cases the thermodynamics of adsorption has been carried out by means of B3LYP-D2 method we adopted all along the paper, also M06 and PBE0-D3 results are reported in table S1 in Supplementary Information Section. For most plausible catalytic species (according to traditional literature) Ti_2Cl_8 and $TiCl_4$ on site E spectroscopic simulations, both IR and Raman have been performed. In the case of dimer even though, at the adopted ratio N/M between $MgCl_2$ formula units and $TiCl_4$ molecules, GA and previous ΔG_{ads} estimates may reasonably exclude the occurrence of that site, we performed spectroscopic studies to identify possible features typical of that way of binding particularly in relation with monomeric $TiCl_4$ fingerprint on tetracoordinated site. In the following subsections, we analyze to which extent exposed tetracoordinated and pentacoordinated Mg sites are distinguishable in IR and/or Raman spectra and the effect of adsorption of different precatalytic complex Ti_xCl_y on those bands, to discuss whether or not it is possible to obtain an indirect vibrational evidence of the presence of precatalytic

species on specific sites.

1. Vibrational characterization of tetrahedral $TiCl_4$

Gas phase molecule (T_d point group) shows nine vibrational modes; we discuss the relevant frequencies: a triple degenerate F_2 mode at 516 cm^{-1} (experimental 500 cm^{-1} for liquid $TiCl_4$) active in Raman (weak) and Far-IR (strong), the totally symmetric A_1 mode at 405 cm^{-1} (exp. 396 cm^{-1}), Raman active and very strong as generally expected for A_1 modes in Raman, the F2 mode at 146 cm^{-1} (exp. 143 cm^{-1}), very weak in IR and medium in Raman, the doubly degenerate E mode at 121 cm^{-1} (experimental 119 cm^{-1}) active only in Raman (medium).

2. IR characterization of $MgCl_2$ and $MgCl_2/TiCl_4$

The vibrational spectrum of naked nanoplatelets $50MgCl_2$ and $50MgCl_2$* are reported in Figure 4 (top panels). The spectrum extends from 200 to 550 cm^{-1}. In the spectrum we can clearly identify a low wave-number region in the range 235-360 cm^{-1} that comes from bulk modes. Although this spectral region appears strongly dependent on the shape of the nanoplate, on the number and type of edge ions (compare spectra of $MgCl_2$ and $MgCl_2$* reported in Figure 4), some common features can be recognized:
i) a region between 250-270 cm^{-1} (a tail in the spectra of Figures 4) mainly due to vibrations involving hexacoordinate ions;
ii) a strong peak at 275-280 cm^{-1} and a couple of weak signals at 328 and 340 cm^{-1} due to bulk-like modes coupled with vibrations of T and P sites.
The spectral region between 360 and 500 cm^{-1} is instead not shape dependent. The vibrational analysis of this region permits to attribute distinctive features to P and T Mg^{2+} ions:
iii) the modes in the range 382 -398 $cm^{-1}$with a maximum at 393 cm^{-1} are due to the movement that brings closer the two Mg of a four-membered Mg-Cl-Mg-Cl cycles, this mode can be easily compared to vibration falling at 393 cm^{-1} typical of (104) surfaces;
iv) the modes falling at 429 cm^{-1} and at 436-459 cm^{-1} with a maximum at 445 cm^{-1} typical of tetracoordinated Mg^{2+} ions (absorption at 435 cm^{-1} is present in the case of

(110) surfaces). Notice the larger intensity of the 445 cm^{-1} band for $50MgCl_2$*, consistent with the larger fraction of the T site as compared to $50MgCl_2$.

To complete the picture we find that the Mg-Cl stretching of a tetrahedral termination falls at 493 cm^{-1} .

Simulated IR spectrum of $TiCl_4$ adsorption on T site of $50MgCl_2$ and $50MgCl_2$*, are reported in the bottom panels of Figure 4. In both cases we analyze only the spectral regions of interest for Ti species and omit to explain about the bands associated to bulk movements. The presence of $TiCl_4$ produces:

v) a reduction of the intensity of the band at 448 cm^{-1} related to tetracoordinated Mg^{2+} and concomitantly the appearance of two new bands at 465 and 485 cm^{-1}, associated to the symmetric and antisymmetric stretching of the Ti-Cl bonds derived from the F2 mode at 500 cm^{-1} that splits into more components due to the symmetry reduction;

vi) the band at 429 cm^{-1} associated to isolated T sites remains unperturbed;

vii) an increase of the intensity of the signals in the region between 311 cm^{-1} and 322 cm^{-1} due to both symmetric and antisymmetric stretching of the bonds formed between the Cl atoms of $TiCl_4$ and the anchoring Mg atoms of the support;

viii) the appearance of an extra weak band at 278 cm^{-1} can be due to a frustrated rocking of $TiCl_4$ moiety on support.

The findings are in agreement with infrared transmission spectra of $MgCl_2/TiCl_4$ precatalyst reported by Ystenes[39] where distinct bands near 450 cm^{-1} appear.

3. Raman characterization of $MgCl_2$ and $MgCl_2/TiCl_4$

Unlike IR spectra, Raman spectra appear much less sensitive to the nanoplate shape. By comparing spectra of $50MgCl_2$ and $50MgCl_2$* (see panels a and c of Figure 5) we see that they are characterized by similar signals:

i) a very weak mode at 161 cm^{-1} together with other weak and unidentified lines in the 100-200 cm^{-1} range all due to bulk movements;

ii) a very intense peak at 263-267 cm^{-1} and a slightly less intense one at $\sim$ 300 cm^{-1} due to bulk and terminations models coupled together (a very strong band at 243 cm^{-1} and a weak band at 157 cm^{-1}, were also identified by Zerbi et al.[36] for naked ball-milled $MgCl_2$

particles);
iii) a weak mode at 384 cm^{-1} (termination modes);
iv) signals at 429 and 445 cm^{-1} (assigned to T mode in the IR spectra) are here hardly detectable because of their very low intensity.

Upon $TiCl_4$ adsorption the Raman spectra undergo a spectacular change (bottom panels in Figure 5): the bulk modes at 161 cm^{-1}, 263-267 cm^{-1} (bulk and terminations) and 384 cm^{-1} (termination modes) drastically reduce their intensities and two new intense lines appear at 465 and 484 cm^{-1}. Zerbi[36] et al. identified similar bands for a ball-milled $TiCl_4$/ $MgCl_2$ precatalyst. In particular they reported two weak signals at 157 and 243 cm^{-1} and two neat lines at 449 and 464 cm^{-1}; the latter lines were assigned to the $TiCl_4$ F2 mode also Raman active. Thus, the $TiCl_4$ symmetric and antisymmetric stretchings, very weak in IR spectra, appear as the dominant bands in the Raman spectra providing indeed an unambiguous fingerprint of the presence of the adduct.
The effect of $TiCl_4$ coverage (compare $50MgCl_2/3TiCl_4$ and $50MgCl_2$*/$TiCl_4$ spectra, panels b and d in Figure 5) can be easily traced by comparing the relative intensities of the bulk like bands (in the 260-300 cm^{-1} spectral region) and the intensities of the $TiCl_4$ signals; note in addition the almost complete annihilation of the 384 cm^{-1}, irrespective of the $TiCl_4$ coverage.

4. IR and Raman characterization of Ti_2Cl_8 dimer

We modeled Ti_2Cl_8 on site E; the simulated IR and Raman spectra are reported in Figure 6. We focus on the 450-495 cm^{-1} spectral region where the signals from the monomeric species were observed (a detailed analysis of the spectra is reported in the Supplementary Information). In IR spectrum, Ti_2Cl_8 produces a triplet of bands at 458, 476, 495 cm^{-1} that, although of low intensity, can eventually overlap those of the monomer. A set of three intense bands is also observed in Raman, at 458, 476 and 495 cm^{-1} but redshifted by ~ 10 cm^{-1} with respect to $TiCl_4$ vibrations; thus, the Raman features of the two adducts appear distinguishable from each other as they differ in shape and frequency values.

IV. CONCLUSIONS

Model nanoclusters of naked $MgCl_2$ and $MgCl_2/TiCl_4$ support have been obtained by means of a non-empirical structure determination method exploiting an evolutionary algorithm. The bare 50 $MgCl_2$ predominantly exposes pentacoordinated sites (P) of the kind of Mg^{2+} sites typically exposed by (104), (107) (012) surfaces and isolated tetracoordinated sites (T). In the presence of $TiCl_4$, a significant increase in the fraction of T sites is found in $50MgCl_2/3TiCl_4$ system, T sites are present as isolate site but mostly as couples and close to rows of P sites. The couple of adjacent T sites allows the binding of $TiCl_4$ molecules in octahedral geometry locally reproposing the edges between adjacent faces exposing pentacoordinated and tetracoordinated Mg^{2+} ions, respectively. Those features represent the topological preconditions to generate favourite sites for strong $TiCl_4$ adsorption (such as the (110)/(104), (110)/(012) and (110)/(015) as reported in previous literature).

The proposed model sites, probed by CO, satisfy the requirement of the well-assessed existence of multiple sites (i.e. P and T sites) in the catalytic mixtures and, at the same time, the superposition of vibrational responses of multiple sites differing by only few cm^{-1}, is perfectly in line with the presence of two bands differing about 20 cm^{-1} in FT-IR spectra in the ν(CO) region on ball-milled $MgCl_2$ samples. CO molecules on nanoplates can successfully probe T sites but cannot distinguish between T sites in different environment (that is between isolated or adjacent sites); the non-negligible increases of adsorption enthalpies and frequencies shifts on nanoplate sites (by 15-20 cm^{-1}), reveal the presence of stronger acidic sites on highly nanostructured support with respect to the homologous ideal surfaces.

The outcomes of IR and even more of Raman simulations on $MgCl_2/TiCl_4$ molecular clusters appear to be of pivotal importance. In IR spectra, the presence of $TiCl_4$ mainly causes the reduction of the intensity of the band at 448 cm^{-1} related to couples of tetracoordinated Mg^{2+} and concomitantly the appearance of two new bands at 465 and 485 cm^{-1}, associated to the symmetric and antisymmetric stretching of the Ti-Cl bonds. The bands are well separated from those of both isolated $TiCl_4$ and bare $MgCl_2$ but unfortunately, they are very weak in Far-IR spectra in comparison with the vibrations of the support. On the contrary in Raman spectra, the two very intense lines of $TiCl_4$ at 465 and 485 cm^{-1}, appear as the dominant bands providing indeed an unambiguous fingerprint of the presence of the adduct. Indeed, the aforementioned bands at 465 cm^{-1} and 485 cm^{-1} due to the symmetric and

antisymmetric stretching of the two "terminal Chlorines" bound to Titanium undoubtedly allow us to identify the presence of $TiCl_4$ with an octahedral coordination on a tetracoordinated Mg^{2+} in really nanostructured samples of ZN catalysts, in fact they fall in a spectral region that is far from both bulk modes and organic functional groups like the ones adopted as internal and external donors. When we pass to dimer Ti_2Cl_8 on P sites again the Raman spectrum is highly informative, that can be particularly ascribed to the Ti-Cl-Ti bridges. The features of monomeric and dimeric adducts are different in shapes and are also well separated by about 10 cm^{-1}.

The present manuscript provides strong evidence that structural and vibrational simulation of catalysts, by means of truly nanosized models together with machine learning methodology is a powerful tool to establish, at the atomic level, the occurrence of catalytic sites mainly when they reside at defective positions i.e. terminations and edges between "perfect surfaces", to better establish the acidity of multiple sites and to discriminate different catalytic adducts.

The accuracy of the simulated data, the reliability and the easily affordable cost of the calculation by machine learning algorithms support this new combined methodology.

Supporting Information

Details of the adopted DFT methodology. Adsorption energies through other density functionals and complementary material for spectroscopic characterization of Ti_2Cl_8 dimer.

ACKNOWLEDGEMENTS

Access to the HPC resources of CINECA has been appreciated. ISIS Rutherford Appleton Laboratory UKRI, NScD Oak Ridge National Laboratory, European Spallation for experiments and SCARF Scientific Computing Department, STFC Rutherford Appleton Laboratory for computer facilities. Dr. Svemir Rudic and Jonatan Roddom are kindly acknowledged for technical support. Access to the HPC resources of CINES/IDRIS/TGCC obtained thanks to the grant 2020-[A0080810471] made by GENCI is also warmly acknowledged. The work of Gentoku Takasao was supported by JSPS KAKENHI Grant Number JP20J15042.

corresponding authors*: maddalena.damore@unito.it,taniike@jaist.ac.jp

Figures

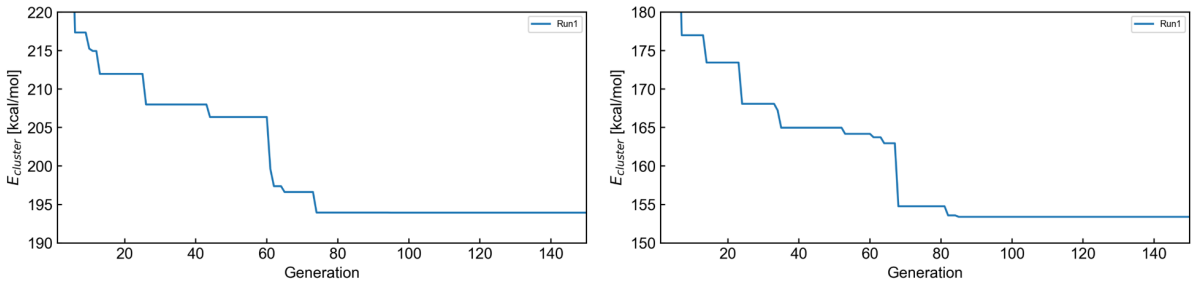

FIG. 1: Evolutionary progress plot for the structure determination of naked $50MgCl_2$ (left panel) and $50MgCl_2/3TiCl_4$ (right panel). The energy of the best-of-generation individual (i.e., the most stable structure in a generation) is plotted against the generation.

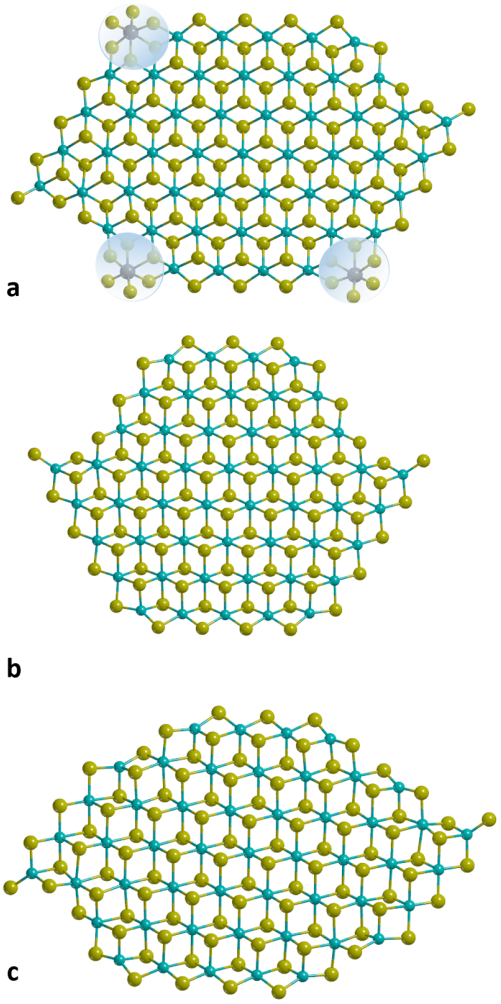

FIG. 2: Nanoplatelet with three adsorbed $TiCl_4$ moieties ($50MgCl_2/TiCl_4$) as obtained by machine learning methodology described in the text (panel a); model of naked $MgCl_2$ nanoplatelet obtained by the same methodology without $TiCl_4$ ($50MgCl_2$) (panel b); nanoplatelet obtained by the first one after removal of the three adsorbed $TiCl_4$ moieties ($50\ MgCl_2{}^*$) (panel c). Structures have been optimized at B3LYP-D2/TZVP level. Chlorine, Magnesium and Titanium atoms are shown in green, yellow and dark grey, respectively. In panel a terminations exposing 4-coordinated Mg^{2+} sites as the ones belonging to (110) covered by $TiCl_4$ in octahedral coordination are enclosed in shaded spheres.

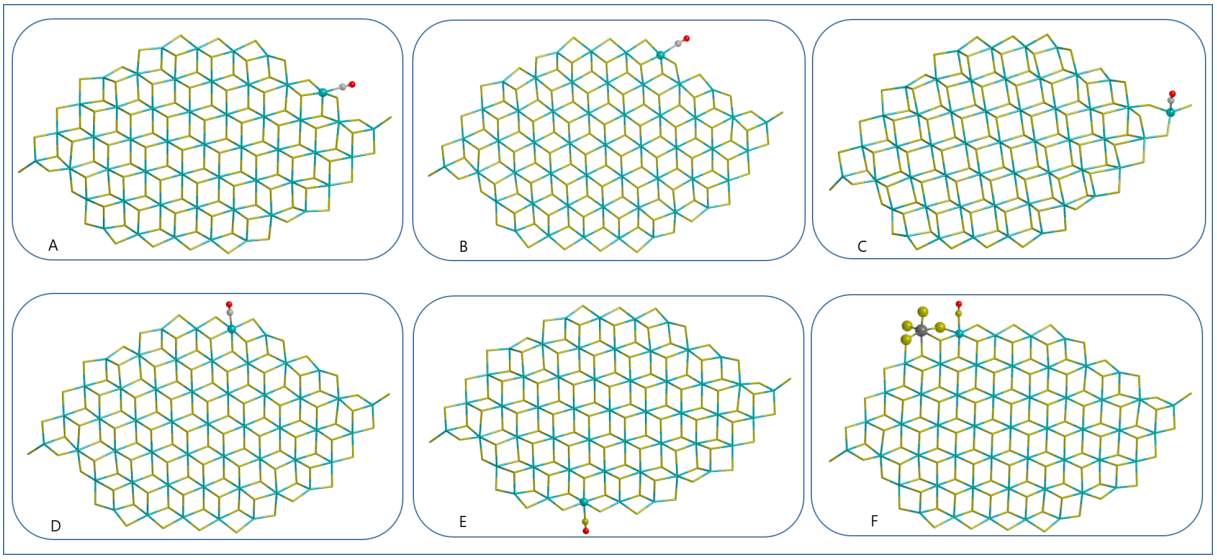

FIG. 3: Optimized CO probed $MgCl_2$ nanoplates ($50MgCl_2$* cluster with CO adsorbed on different sites), minima are reported for each unsaturated site of Mg^{2+}. Chlorine and Magnesium atoms are shown in green and yellow colors, respectively. C, O atoms of adsorbed CO are shown in black and red respectively, they are represented as balls along with the adsorbing Mg^{2+} site. All the rest of atoms belonging to nanoplatelet and not involved in the adsorption process are represented as sticks. (A) CO adsorption on tetracoordinated 110-like Mg^{2+} and next to a tetrahedral site. CO adsorbed on 110-like Mg^{2+} model is reported in (B) and on tetrahedral site in (C). Model of CO adsorption on penta-coordinated Mg^{2+} close to tetracoordinated 110-like Mg^{2+} (D) and penta-coordinated Mg^{2+} (E). Panel (F) sketches the adsorption of CO close to an adsorbed $TiCl_4$ in its octahedral configuration. All calculations were done by employing B3LYP functional including D2 type correction and TZVP basis set and QZVP type basis set on CO moiety.

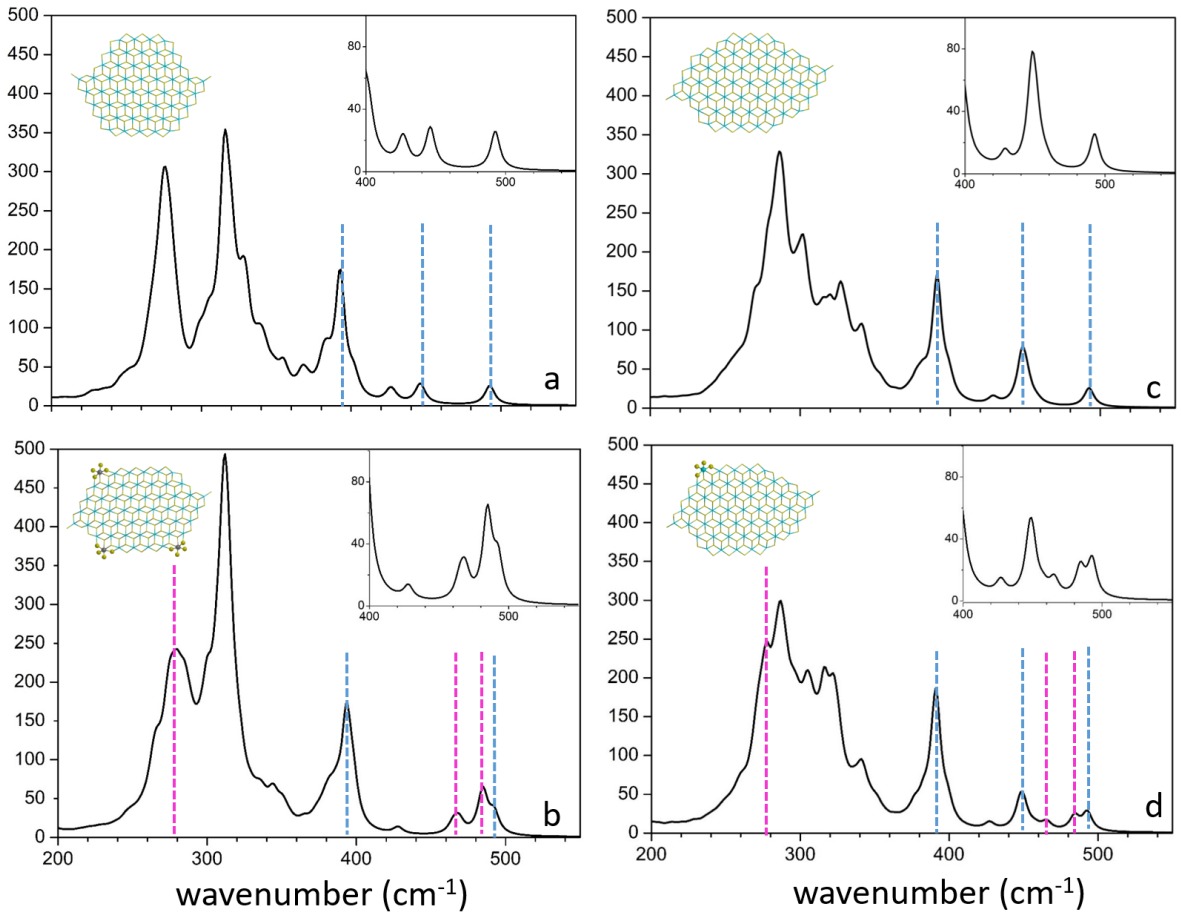

FIG. 4: Simulated IR spectra at B3LYP-D2/TZVP level of calculation of: both naked nanoplatelet and 50$MgCl_2$/$TiCl_4$ system as obtained by genetic algorithm (a and b panels respectively); naked cluster reoptimized after removal of the three $TiCl_4$ molecules (50$MgCl_2$*) and with one $TiCl_4$ molecule adsorbed on site B of the same cluster (c and d panels respectively). Peaks of interest discussed in the text are indicated by dashed lines: in blue color for support modes, pink for typical $TiCl_4$ modes, respectively. The insets in each graph clearly report data in the range of frequency 400 - 550 cm^{-1}. Simple models of adducts are also reported: atoms belonging to the nanoplatelet and not involved in the adsorption process are represented as sticks whereas atoms of $TiCl_4$ molecules as balls; Chlorine and Titanium atoms are shown in green and dark grey, respectively.

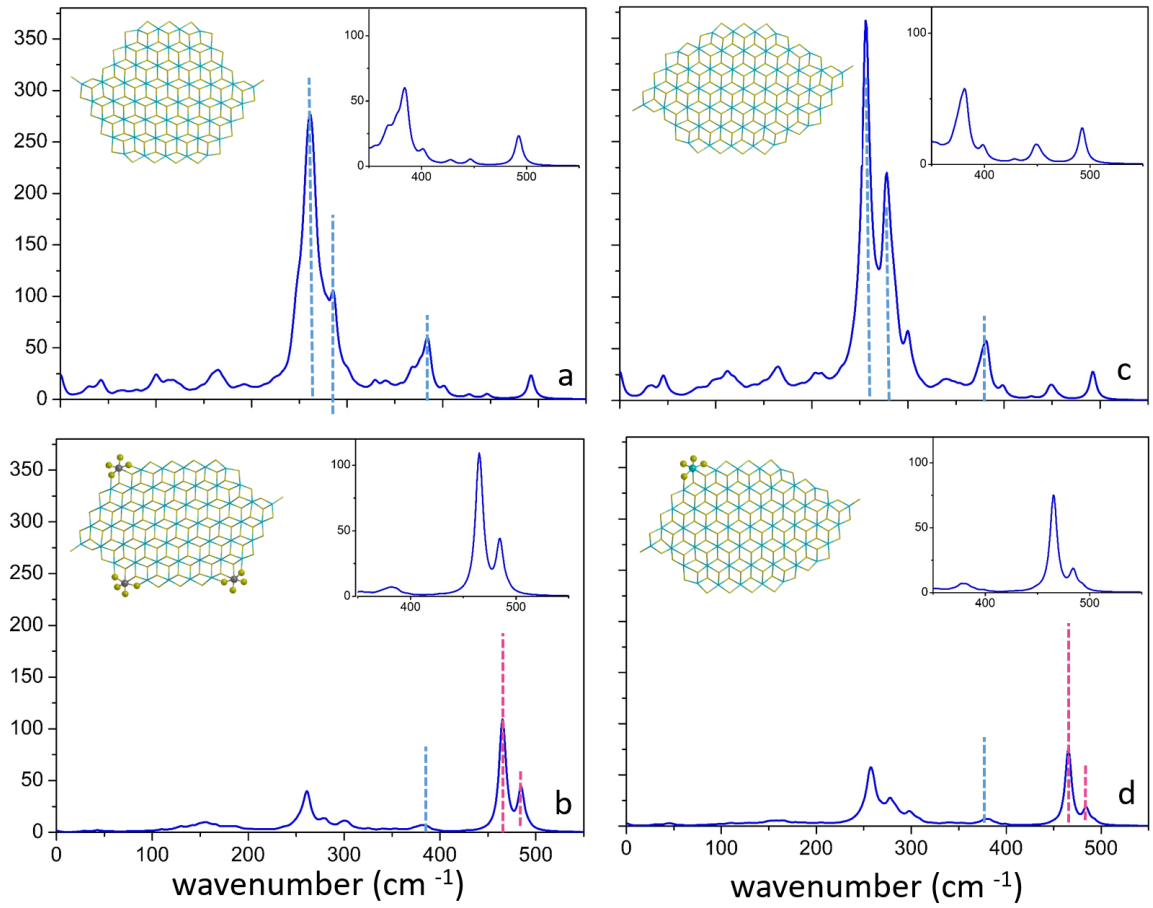

FIG. 5: Simulated Raman spectra at B3LYP-D2/TZVP level of calculation of: naked 50 $MgCl_2$ cluster (panel a) and $50MgCl_2/3TiCl_4$ (i.e. 3 $TiCl_4$ molecules chemisorbed on type-B sites of the cluster) (panel b) as obtained by genetic algorithm; $50MgCl_2$* (panel c) and $50MgCl_2$*$/1TiCl_4$ (i.e. one $TiCl_4$ molecule chemisorbed on type-B sites of the cluster) (panel d). Simple models of adducts are also reported: atoms belonging to the nanoplatelet and not involved in the adsorption process are represented as sticks whereas atoms of $TiCl_4$ molecules as balls; Chlorine and Titanium atoms are shown in green and dark grey, respectively.

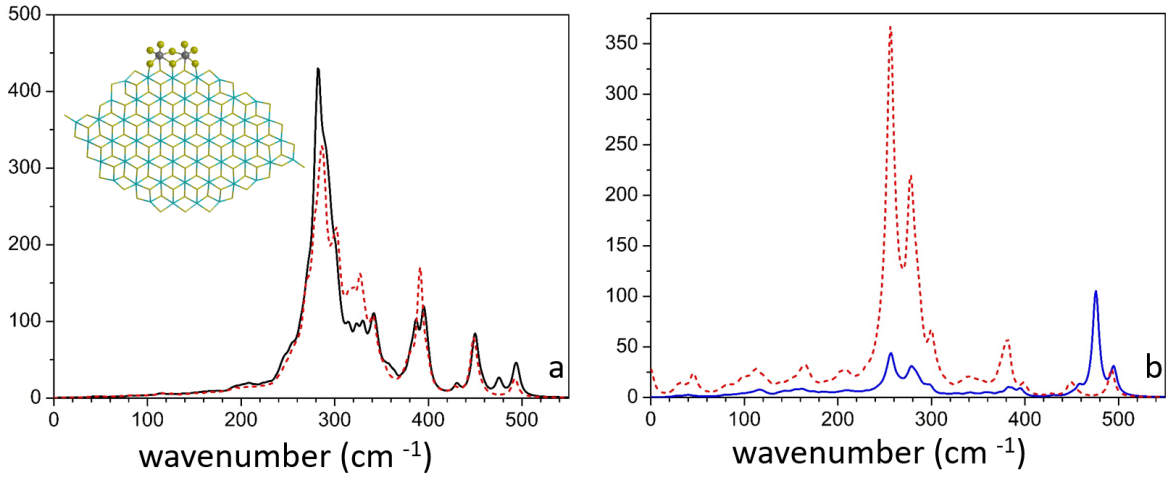

FIG. 6: Simulated IR (panel a) and Raman (panel b) spectra at B3LYP-D2/TZVP level of calculation of the dimer Ti_2Cl_8 epitactically bound to site E of $50MgCl_2{}^*$ cluster. In each panel the response relative to naked nanocluster is also reported in dashed red line.

Tables

TABLE I: Distribution of Mg^{2+} cations with different coordination numbers or symmetry, after removing $TiCl_4$ in structures reported in Fig.1. The system indicated as $50MgCl_2^*$ corresponds to the $50MgCl_2/TiCl_4$ after removing the 3 $TiCl_4$ molecules in the cluster reported in Fig.1, panel a.

System	distribution of Mg^{2+} cations (%)			
	T_d	4-fold	5-fold	6-fold
$50MgCl_2$	4	8	30	58
$50MgCl_2/TiCl_4$ ($50MgCl_2^*$)	4	14	20	62
Difference	0	6	-10	4

TABLE II: Energetics of CO adsorption on each cluster site as reported in Fig.1 (energies in kJ/mol) (G at 100 K). Predicted shift $\Delta\nu$(CO) in cm^{-1} with respect to ν(CO) in gas phase and computed intensity (Km/mol) for CO molecule adsorbed on different $50MgCl_2$* cluster. At the employed level of computation, we predicted for the A mode ν(CO)=2201.3 cm^{-1} in gas phase and Intensity= 78.45 Km/mol. In the case F the reference structure is the nanoplatelet with one $TiCl_4$ molecule adsorbed on site B. The results are compared with those obtained on regular surfaces. All calculations were done by employing B3LYP functional including D2 type correction and TZVP basis set and QZVP type basis set on CO moiety.

Site	ΔE_{ads}	ΔG_{ads}	$\Delta\nu$	Intensity	surfaces	$\Delta E_{ads_{surf}}$	$\Delta G_{ads_{surf}}$	$\Delta\nu$
A	-41.7	**-25.5**	73.9	87.7	(110)	-40.2	-14.5	63.8
B	-41.3	**-25.1**	73.6	86.1				
C	-31.8	**-16.7**	61.5	93.7	-	-	-	-
D	-36.5	**-20.8**	63.6	104.5	(104),(107)	-41.0,-47.2	-13.9,-18.1	53.6,54.2
E	-36.2	**-20.3**	61.8	105.8	(104),(107)	-41.0,-47.2	-13.9,-18.1	53.6,54.2
F	-42.3	**-25.6**	71.3	81.9	-	-	-	-

References

[1] Correa, A.; Bahri-Laleh, N.; Cavallo, L. How Well Can DFT Reproduce Key Interactions in Ziegler–Natta Systems? *Macromol. Chem. Phys.* **2013**, *214*, 1980–1989.

[2] Corradini, P.; Barone, V.; Fusco, R.; Guerra, G. Analysis of models for the Ziegler-Natta stereospecific polymerization on the basis of non-bonded interactions at the catalytic site—I. The Cossee model. *Eur. Polym. J.* **1979**, *15*, 1133–1141.

[3] Boero, M.; Parrinello, M.; Terakura, K. First Principles Molecular Dynamics Study of Ziegler-Natta Heterogeneous Catalysis. *J. Am. Chem. Soc.* **1998**, *120*, 2746–2752.

[4] Boero, M.; Parrinello, M.; S. Hüffer, S.; Weiss, H. First Principles Study of Propene Polymerization in Ziegler-Natta Heterogeneous Catalysis. *J. Am. Chem. Soc.* **2000**, *122*, 501–509.

[5] Monaco, G.; Toto, M.; Guerra, G.; Cavallo, L. Geometry and stability of titanium chloride species adsorbed on the (100) and (110) cuts of the $MgCl_2$ support of the heterogeneous Ziegler-Natta catalysts. *Macromolecules* **2000**, *33*, 8953–8962.

[6] Boero, M.; Parrinello, M.; Weiss, H.; Hüffer, S. A First Principles Exploration of a Variety of Active Surfaces and Catalytic Sites in Ziegler-Natta Heterogeneous Catalysis. *J. Phys. Chem. A* **2001**, *105*, 5096–5105.

[7] Seth, M.; Margl, P. M.; Ziegler, T. A Density Functional Embedded Cluster Study of Proposed Active Sites in Heterogeneous Ziegler-Natta Catalysts. *Macromolecules* **2002**, *35*, 7815–7829.

[8] Taniike, T.; Terano, M. Reductive Formation of Isospecific Ti Dinuclear Species on a $MgCl_2$ (110) Surface in Heterogeneous Ziegler-Natta Catalysts. *Macromolecular rapid communications* **2008**, *29*, 1472–1476.

[9] D'Amore, M.; Credendino, R.; Budzelaar, P. H. M.; Causá, M.; Busico, V. A Periodic Hybrid DFT Approach (Including Dispersion) to $MgCl_2$-supported Ziegler-Natta catalysts 1:$TiCl_4$ Adsorption on $MgCl_2$ Crystal Surfaces. *J. Catal.* **2012**, *286*, 103–110.

[10] Breuza, E.; Antinucci, G.; Budzelaar, P. H. M.; Busico, V.; Correa, A.; Ehm, C. $MgCl_2$-supported Ziegler-Natta catalysts: A DFT-D 'flexible-cluster' approach. $TiCl_4$ and probe donor adducts. *Int. J. Quantum Chem.* **2018**, *118*, e25721.

[11] Breuza, E.; Antinucci, G.; Budzelaar, P. H. M.; Busico, V.; Correa, A.; Ehm, C. $MgCl_2$-Supported Ziegler–Natta Catalysts: a DFT-D "Flexible-Cluster" Approach to Internal Donor Adducts. *J. Phys. Chem. C* **2018**, *122*, 9046–9053.

[12] Capone, F.; Rongo, L.; D'Amore, M.; Budzelaar, P. H. M.; Busico, V. A Periodic Hybrid DFT Approach (Including Dispersion) to $MgCl_2$-supported Ziegler-Natta catalysts 2: Model Electron Donor Adsorption on $MgCl_2$ Crystal Surfaces. *J. Phys. Chem. C* **2013**, *117*, 24345–24353.

[13] Credendino, R.; Pater, J. T. M.; Correa, A.; Morini, G.; Cavallo, L. Thermodynamics of Formation of Uncovered and Dimethyl Ether Covered $MgCl_2$ Crystallites. Consequences in the Structure of Ziegler-Natta Heterogeneous Catalysts. *J. Phys. Chem. C* **2011**, *115*, 13322–13328.

[14] D'Amore, M.; Thushara, K.; Piovano, A.; Causá, M.; Bordiga, S.; Groppo, E. Surface Investigation and Morphological Analysis of Structurally Disordered $MgCl_2$ and $MgCl_2/TiCl_4$ Ziegler-Natta Catalysts. *ACS Catal.* **2016**, *6*, 5786–5796.

[15] Wada, T.; Takasao, G.; Piovano, A.; D'Amore, M.; Thakur, A.; Chammingkwan, P.; Bruzzese, P. C.; Terano, M.; Civalleri, B.; Bordiga, S.; et al. Revisiting the Identity of δ-$MgCl_2$: Part I. Structural Disorder Studied by Synchrotron X-Ray Total Scattering. *J. Catal.* **2020**, *385*, 76–86.

[16] Piovano, A.; D'Amore, M.; Wada, T.; Bruzzese, P. C.; Takasao, G.; Thakur, A.; Chammingkwan, P.; Terano, M.; Civalleri, B.; Bordiga, S.; et al. Revisiting the Identity of δ-$MgCl_2$: Part II. Morphology and Exposed Surfaces Studied by Vibrational Spectroscopies and DFT Calculation. *J. Catal.* **2020**, *387*, 1–11.

[17] Credendino, R.; Liguori, D.; Fan, Z.; Morini, G.; Cavallo, L. A Unified Model Explaining Heterogeneous Ziegler-Natta Catalysis. *ACS Catal.* **2015**, *5*, 5431–5435.

[18] D'Amore, M.; Piovano, A.; Vottero, E.; Rudic, S.; Groppo, E.; Bordiga, S.; Civalleri, B. Insights on inelastic neutron scattering data of $MgCl_2$ ZN-catalyst support from *ab initio* modelling of nano-sized and disordered models. *ACS Appl. Nano Mater.* **2020**, *3*, 11118–11128.

[19] Thushara, K.; D'Amore, M.; Piovano, A.; Bordiga, S.; Groppo, E. The Influence of Alcohols in Driving the Morphology of Magnesium Chloride Nanocrystals. *ChemCatChem* **2017**, *9*, 1782–1787.

[20] Zakharov, V.; Paukshtis, E. A.; Mikenas, T. B.; Volodin, A. M.; Vitus, E. N.; Potapov, A. Surface acidic sites of highly disperse magnesium chloride: IR and ESR spectroscopy studies. *Macromol. Symp.* **1995**, *89*, 55–61.

[21] Takasao, G.; Wada, T.; Thakur, A.; Chammingkwan, P.; Terano, M.; Taniike, T. Machine Learning-Aided Structure Determination for $TiCl_4$-Capped $MgCl_2$ Nanoplate of Heterogeneous Ziegler-Natta Catalyst. *ACS Catal.* **2019**, *9*, 2599–2609.

[22] Takasao, G.; Wada, T.; Thakur, A.; Chammingkwan, P.; Terano, M.; Taniike, T. Insight into Structural Distribution of Heterogeneous Ziegler–Natta Catalyst from Non-empirical Structure Determination. *J. Catal.* **2021**, *394*, 299–306.

[23] Wada, T.; Funako, T.; Thakur, A.; Matta, A.; Terano, M.; Taniike, T. Structure-performance relationship of $Mg(OEt)_2$-based Ziegler-Natta catalysts. *J. Catal.* **2021**, *389*, 525–532.

[24] Taniike, T.; Terano, M. Coadsorption Model for First-Principle Description of Roles of Donors in Heterogeneous Ziegler-Natta Propylene Polymerization. *J. Catal.* **2012**, *293*, 39–50.

[25] Hohenberg, P.; Kohn, W. Inhomogeneous Electron Gas. *Phys. Rev.* **1964**, *136*, B864.

[26] Kohn, W.; Sham, L. J. Self-Consistent Equations Including Exchange and Correlation Effects. *Phys. Rev.* **1965**, *140*, A1133.

[27] Becke, A. D. Density-Functional Thermochemistry. III. The Role of Exact Exchange. *J. Chem. Phys.* **1993**, *98*, 5648–5652.

[28] Lee, C.; Yang, W.; Parr, R. Development of the Colle-Salvetti Correlation-Energy Formula Into a Functional of the Electron Density. *Phys. Rev. B* **1988**, *37*, 785–789.

[29] Dovesi, R.; Erba, A.; Orlando, R.; Zicovich-Wilson, C. M.; Civalleri, B.; Maschio, L.; Rérat, M.; Casassa, S.; Baima, J.; Salustro, S.; et al. Quantum-Mechanical Condensed Matter Simulations with CRYSTAL. *WIREs Computational Molecular Science* **2018**, *8*, e1360.

[30] Dovesi, R.; Pascale, F.; Civalleri, B.; Doll, K.; Harrison, N. M.; Bush, I.; D'Arco, P.; Noël, Y.; Rérat, M.; Carbonnière, P.; et al. The CRYSTAL code, 1976–2020 and beyond, a long story. *The Journal of Chemical Physics* **2020**, *152*, 204111.

[31] Grimme, S. S. Semiempirical GGA-Type Density Functional Constructed with a Long-Range Dispersion Correction. *J. Comput. Chem.* **2006**, *27*, 1787–1799.

[32] Grimme, S.; Antony, J.; Ehrlich, S.; Krieg, H. A Consistent and Accurate Ab Initio Parametrization of Density Functional Dispersion Correction (DFT-D) for the 94 Elements H-Pu. *J. Chem. Phys.* **2010**, *132*, 5648–5652.

[33] Fornaro, T.; Brucato, J. R.; Feuillie, C.; Sverjensky, D. A.; Hazen, R. M.; Brunetto, R.; D'Amore, M.; Barone, V. Binding of Nucleic Acid Components to the Serpentinite-Hosted Hydrothermal Mineral Brucite. *Astrobiology* **2018**, *18*, 989–1007.

[34] Signorile, M.; Vitillo, J. G.; D'Amore, M.; Crocellà, V.; Ricchiardi, G.; Bordiga, S. Characterization and Modeling of Reversible CO_2 Capture from Wet Streams by a MgO/Zeolite Y Nanocomposite. *J. Phys. Chem. C* **2019**, *123*, 17214–17224.

[35] Civalleri, B.; Maschio, L.; Ugliengo, P.; Zicovich-Wilson, C. M. Role of dispersive interactions in the CO adsorption on MgO(001): periodic B3LYP calculations augmented with an empirical dispersion term. *Phys. Chem. Chem. Phys.* **2010**, *12*, 6382–6386.

[36] Brambilla, L.; Zerbi, G.; Nascetti, F., S. andPiemontesi; Morini, G. Experimental and calculated Vibrational spectra and structure of Ziegler-Natta catalyst precursor: 50/1 comilled $MgCl_2$-$TiCl_4$. *Macromol. Symp.* **2004**, *213*, 287–301.

[37] Correa, A.; Credendino, R.; Pater, J.; Morini, G.; Cavallo, L. Theoretical investigation of active sites at the corners of $MgCl_2$ crystallites in supported ziegler-natta catalysts. *Macromolecules* **2015**, *45*, 3695–3701.

[38] Bazhenov, A.; Linnolahti, M.; Pakkanen, T. A.; Denifl, P.; Leinonen, T. Modeling the Stabilization of Surface Defects by Donors in Ziegler–Natta Catalyst Support. *J. Phys. Chem. C* **2014**, *118*, 4791–4796.

[39] Bache, Ø.; Ystenes, M. Double-Chamber Flow Cell for in Situ Infrared Spectroscopy Studies of Chemical Reactions in Ziegler-Natta Catalyst Systems. *Appl. Spectrosc.* **1994**, *48*, 985–993.